Balanced MEMS loudspeaker: Coulomb forces vs. viscosity of air and squeeze film damping

Anton Melnikov[1,*], Hermann A. G. Schenk[2], Michael Stolz[1,3], Andreas Mrosk [1], Lutz Ehrig[2], Franziska Wall[1], Jorge M. Monsalve[1], Maik Ahnert[4], Sergiu Langa[1], Bert Kaiser[1]

[1] *Fraunhofer Institute for Photonic Microsystems IPMS, 01109 Dresden, Germany*

[2] *Arioso Systems GmbH, 01109 Dresden, Germany*

[3] *Brandenburg Technical University Cottbus-Senftenberg BTU, Micro and Nano Systems, Cottbus, Germany*

[4] *Fraunhofer Institute for Machine Tools and Forming Technology IWU, 01187 Dresden, Germany*

[*] *Email: anton.melnikov@ipms.fraunhofer.de*

Abstract

Miniaturized loudspeakers based on MEMS (micro electro-mechanical systems) technology are a current developmental trend for in-ear audio applications. However, when a loudspeaker shrinks to a size of a microelectronic chip, the involved physics starts to differ from the macroscopic world. At one side, an electrostatic MEMS loudspeaker benefits from small electrode gaps leading to high driving forces. At the same time, the fluid dynamics of the air can cause strong damping forces inside the microscopic cavities of a μSpeaker chip. In our presentation, we discuss the influence of the fluid dynamics on the damping of a balanced nanoscopic electrostatic drive (NED) test loudspeaker design. We analyze simulation results and link them to experimental observations done with a high-speed camera. Understanding the various sources of fluid dynamic damping is of high importance for the design of high fidelity MEMS audio transducers.

Introduction

MEMS-based micro-speakers (μSpeakers) are a new and rapidly developing field in electro-acoustics. The recently developed nanoscopic electrostatic drive (NED) technology [1] offers great potential for electrostatic transducers for audio and ultrasound applications. Kaiser *et al.* demonstrated the experimental realization of an all-silicon μSpeaker based on the NED approach [3]. Such loudspeakers can be manufactured by a process that is fully compatible with complementary metal-oxide-semiconductor (CMOS) technology. This paves the way for high-fidelity μSpeakers for in-ear audio playback that are far superior in size and energy efficiency, are based on silicon technology, and have the potential to claim cost leadership in the mass market. A second important step towards practical application was demonstrated by the combination of NED technology with the push-pull drive principle [4]. To build a push-pull NED actuator, a special cantilever structure is required, which poses new challenges for modeling [4, 6]. Recent articles demonstrate experimental, numerical, and analytical approaches to deriving accurate, single-degree-of-freedom models of MEMS-based μSpeakers [9, 5, 8]. Monsalve *et al.* [7] used a finite element method (FEM) as well as the concentrated parameter models mentioned above to extract the non-linear electromechanical parameters for successful loudspeaker equivalent circuit modeling. Usually the lumped-parameter damping experimentally extracted from comparable designs is used to set up the machanical part of the circuit model. Unfortunately, the computational determination of the damping is still a challenge, as it takes into account the microfluidics in the microcavity around the actuator with extremely narrow channels. In addition, the narrow channels are deformed during the actuator movement, which leads to a squeeze film damping. Here we report on the FEM-based determination of the natural frequency and the quality factor of an actuator that was developed to drive a symmetrical MEMS loudspeaker. In addition, we determine the quality factor experimentally with a high-speed camera to validate our FEM results. This offers a deep insight into the fluidic damping and thus enables targeted damping design of comparable actuators.

Methods

High speed camera. A high-speed Photron Fastcam SA1.1 camera was mounted on top of a Leica DM8000 microscope, see Fig. 1a. The details of the actuator dynamics were tracked using a 500x magnification and a frame rate of 50 kfps. A typical micrograph with a frame resolution of 192×160 pixels is shown in Fig. 1b. The actuator was moved mechanically with a tungsten needle of an Imina Tec MiBot and then released into a free oscillation state. In order to record the free oscillation, the recording time of each experiment was 2 ms. No actuation voltage was applied to the actuator during the entire experiment.

Tracking and parameter fit. For the evaluation, the deflection of the actuator is tracked using the Lucas-Kanade method, as provided in the OpenCV Python library. In particular, a single marker is placed on the actuator head (see red marker in Fig. 1(b)) and its trajectory is extracted in the image plane. The deflection in the y-axis was used to calculate the lumped parameters.

In order to get the damped natural frequency and the quality factor from the experiment, a simple pseudoperiodic function is fitted to the tracked deflection

$$u_y(t) = Ae^{-st}\cos(\omega_d t - \phi) + B. \tag{1}$$

The quality factor can be obtained as

$$Q = \frac{\omega_d}{2s} \tag{2}$$

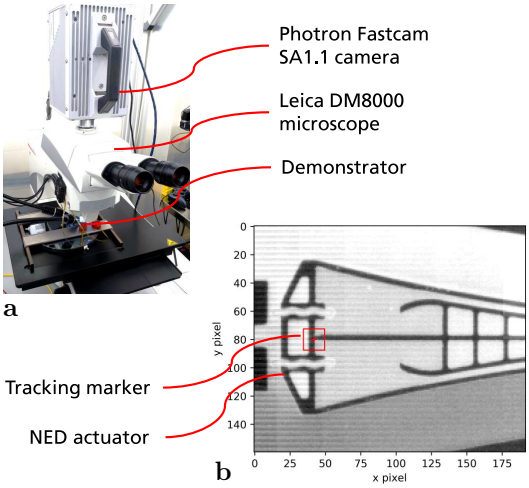

Figure 1: (a) The measurement setup: The Photron Fastcam SA1.1 high-speed camera on top of the Leica DM8000 microscope. (b) A micrograph of the free end of the BNED structure. The red marker shows the position of the pattern tracking used for the extraction of the motion, similar to Ref. [6]

and the damped natural frequency as

$$f_d = \frac{\omega_d}{2\pi}. \tag{3}$$

Finite Element Model. The FEM modeling was implemented with COMSOL Multiphysics 5.6. The structural domain and the acoustic domains are discretized with 3D elements of the second order. The FEM mesh is shown in Fig. 2, where different domains are marked with different colors. The air shown in blue inside the microcavity is modeled using thermoviscous acoustics (linearized Navier-Stokes equation), while the usual pressure acoustics description (Helmholtz equation) is used for the air above the chip (light blue). In addition, the infinite expansion of the open volume above the chip is modeled with a perfectly matched layer (PML) formulation. The silicon (Si) is modeled with anisotropic parameters measured by Hopcroft *et al.* [2] and the air is modeled with standard parameters from COMSOL. The analysis type is a modal analysis that directly specifies the damped natural frequency and the quality factor.

Results

The tracked deflection at the marker shown in Fig. 1 is shown in Fig. 3 as a red solid line with error bars. The error bars are provided by the Lucas-Kanade method implementation. The MiBot needle releases the actuator after approx. 250 μs of the measuring time. When released, a typical pseudo-periodic response of a free damped oscillator is observed. After approx. 1.25 ms of oscillatory movement, the deflection of the actuator falls below the tracking capabilities of the method.

To obtain lumped parameter we fit Eq. (1) to the measured data. The resulting curve is shown in Fig. 3 as dashed black line and matches the measured curve with high accuracy. The extracted damped eigenfrequency f_d and Q factor are given in Tab. 1.

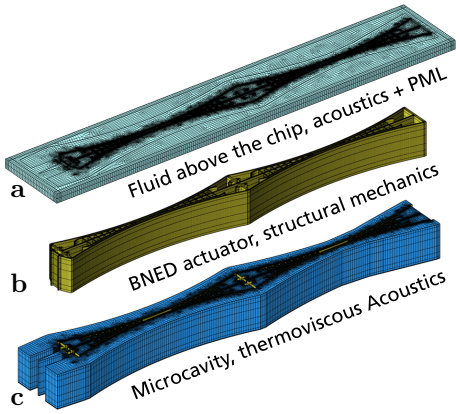

Figure 2: Exploded view of the FEM model of the actuator in the state without a cover wafer. (a) Air domain above the chip. (b) Structural domain including the actuator. (c) Air domain within the microcavity, modeled with thermoviscous acoustics.

Table 1: Caption

	Exp.	FEM	Rel. error
f_d / kHz	4.82	4.76	0.012
Q	3.91	4.01	0.026

The FEM modal analysis provides a damped natural frequency and a quality factor, which are compared with the experimentally obtained parameters in Tab. 1. Experimentally determined and simulated values are very close to one another and the relative error remains below 3 % for both parameters. This leads us to assume that the flow dynamic influence on the system damping is precisely reproduced by our FEM model.

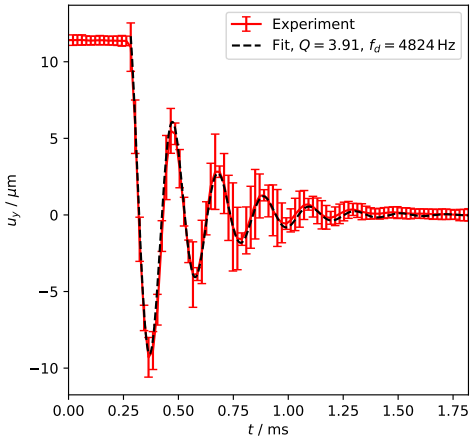

Figure 3: (a) The measurement setup: The Photron Fastcam SA1.1 high-speed camera on top of the Leica DM8000 microscope. (b) A micrograph of the free end of the BNED structure. The red marker shows the pattern tracking location used for the extraction of the movement.

To review the airflow in the microcavities around and inside the actuator the flow velocity in x direction (along the actuator) is shown in Fig. 4. The highest flow velocities are located around the actuator head (see Fig. 4b) and inside the electrostatic gap of cell 1. Such a high flow rate within the gap indicates a significant contribu-

tion from the squeeze film damping during the bending of the entire structure. Therefore, the electrostatic gap, as a long and narrow channel, plays an essential role in the overall damping of the system.

Another important flow direction is that normal to the chip plane. Figure 5 shows the flow rate in the z-direction with additional detailed views of important points. Again, we observe high flow velocities around the actuator head, but in this case the flow is distributed approximately half the length of the cavity. In detailed views (Fig. 5bc), black arrows show the direction vectors of the flow and Hagen-Poiseuille-like profiles can be seen. In addition, the vectors near the actuator surface have a significant y-component that can be traced back to the actuator movement. Figure 5d shows the flow velocity in the center of cell 1, where the highest flow velocities are again within the electrostatic gap. An additional enlargement in Fig. 5e shows the air transport from the electrostatic gap through the clearance to the side cavities.

Even if the analysis of the flow within the microcavity suggests that the electrostatic gap will have a high impact on the overall damping of the system, further quantification would be useful. In order to obtain a performance-related surface contribution, we apply the surface integral

$$P_x = \int_S T_x \dot{u}_x \mathrm{d}S \tag{4}$$

to different surface groups: inner surfaces (including electrostatic gap), clearance surface and outer surfaces, while T_x is the stress tensor component and $\dot{u}_x$ is the surface velocity. Then we normalize the contribution with the maximum value over the directions and surface groups

$$\hat{P}_x = \frac{P_x}{|P_{\max}|}. \tag{5}$$

The resulting normalized contributions separated in real and imaginary parts are shown in Tab. 2. We observe that the imaginary contribution of the inner surfaces dominates and shows a significant contribution from them to the overall system damping. Since Figs. 4 and 5 show high flow velocities in electrostatic gaps, it can be assumed that the high contribution of the inner surfaces is related to the squeeze film damping within the electrostatic gaps. From this it can be concluded that the geometric parameters of the electrostatic gap play an essential role in the damping design of the MEMS loudspeaker.

Conclusion

The damped natural frequency and the quality factor of a BNED actuator were determined experimentally and with the FEM. The FEM results agree with the experiment with a high degree of accuracy. From the numerics it could be concluded that the geometry of the actuator including the electrostatic gap strongly influences the damping of the first eigenmode. This shows how important the actuator geometry is for the damping, while a well designed damping is indispensable for an appropriate μSpeaker design.

This work was supported by Fraunhofer-Zukunftsstiftung.

References

[1] Conrad, H., Schenk, H., Kaiser, B., Langa, S., Gaudet, M., Schimmanz, K., Stolz, M., and Lenz, M. A small-gap electrostatic micro-actuator for large deflections. *Nature Communications 6*, 1, 1–7.

[2] Hopcroft, M. A., Nix, W. D., and Kenny, T. W. What is the Young's Modulus of Silicon? *Journal of Microelectromechanical Systems 19*, 2 (2010), 229–238.

[3] Kaiser, B., Langa, S., Ehrig, L., Stolz, M., Schenk, H., Conrad, H., Schenk, H., Schimmanz, K., and Schuffenhauer, D. Concept and proof for an all-silicon MEMS micro speaker utilizing air chambers. *Microsystems & Nanoengineering 5*, 1 (2019), 1–11.

[4] Kaiser, B., Schenk, H. A. G., Ehrig, L., Wall, F., Monsalve, J. M., Langa, S., Stolz, M., Melnikov, A., Conrad, H., Schenk, H., and Schuffenhauer, D. Electrostatic push-pull bending actuator for low distortion acoustic transducers. *Submitted*.

[5] Melnikov, A., Schenk, H. A. G., Monsalve, J. M., Wall, F., Stolz, M., Mrosk, A., Langa, S., and Kaiser, B. Coulomb-actuated microbeams revisited: experimental and numerical modal decomposition of the saddle-node bifurcation. *Microsystems & Nanoengineering 7*, 1 (2021).

[6] Melnikov, A., Stolz, M., Schenk, H. A. G., Wall, F., Kaiser, B., Mrosk, A., Ehrig, L., Schuffenhauer, D., Monsalve, J. M., Ahnert, M., Langa, S., Conrad, H., and Schenk, H. Nonlinearity of balances MEMS loudspeakers: optical experiments and numerical modeling using time-harmonic signals. *27th International Congress on Sound and Vibration* (2021).

[7] Monsalve, J. M., Melnikov, A., Kaiser, B., Schuffenhauer, D., Stolz, M., Ehrig, L., Schenk, H. A., Conrad, H., and Schenk, H. Large-signal equivalent-circuit model of asymmetric electrostatic transducers. *IEEE/ASME Transactions on Mechatronics* (2021).

[8] Schenk, H. A. G., Melnikov, A., Wall, F., Gaudet, M., Stolz, M., Schuffenhauer, D., and Kaiser, B. Coulomb actuated microbeams revisited: Highly efficient lumped parameter models - a Chebyshev-Edgeworth approach. *Submitted*.

[9] Spitz, B., Wall, F., Schenk, H., Melnikov, A., Ehrig, L., Langa, S., Stolz, M., Kaiser, B., Conrad, H., Schenk, H., and Pufe, W. Audio-Transducer for In-Ear-Applications based on CMOS compatible electrostatic actuators. *MikroSystemTechnik Kongress Proceedings* (2019).

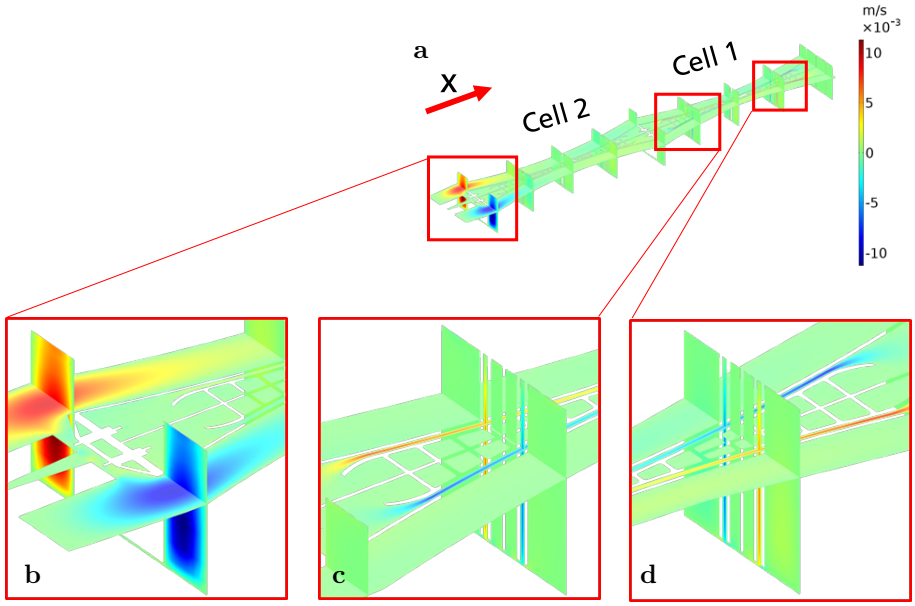

Figure 4: (a) Flow rate in x direction in the microcavity. (b) Detailed view of the flow around the actuator head. (c) Detailed view of the flow in the electrostatic gap of cell 1. (d) Detailed view of the flow in the electrostatic gap of cell 1 close to the actuator anchor

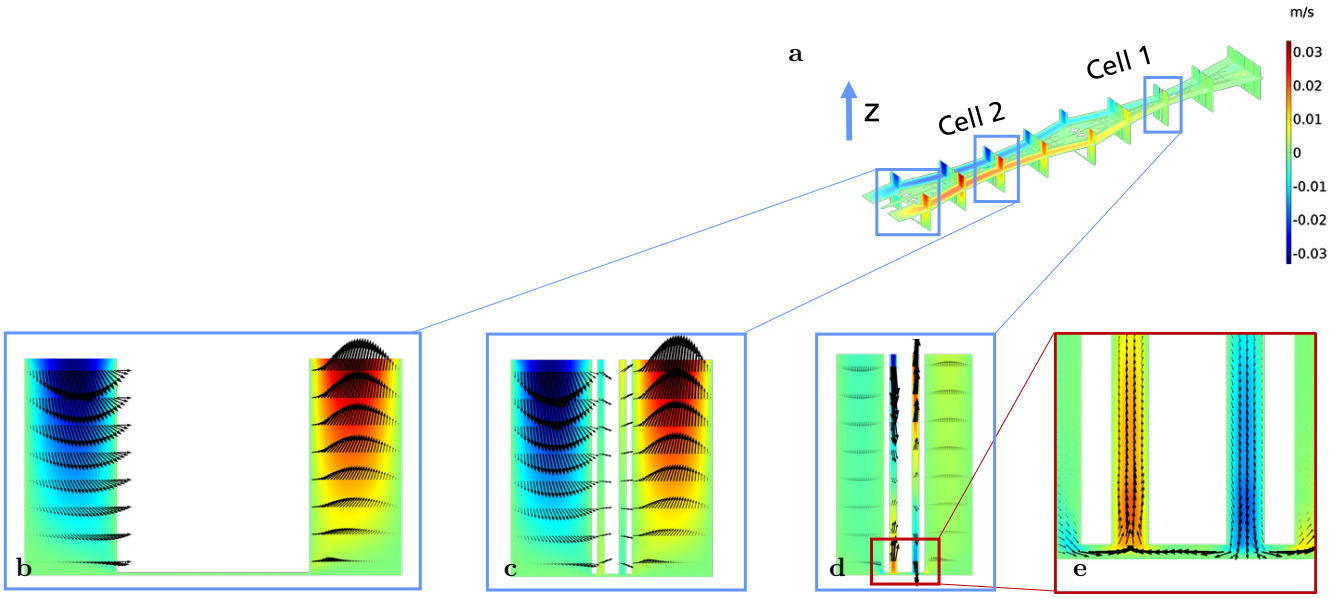

Figure 5: (a) Flow rate in z direction in the microcavity. (b) Detailed view of the flow around the actuator head. (c) Detailed view of the flow in the electrostatic gap in the center of cell 2. (d) Detailed view of the flow in the electrostatic gap in the center of cell 1. (d) Detailed view showing the flow through the clearance below cell 1.

Table 2: Energy related contribution of the stress tensor to the first bending mode.

	$\Re\{\hat{P}_x\}$	$\Im\{\hat{P}_x\}$	$\Re\{\hat{P}_y\}$	$\Im\{\hat{P}_y\}$	$\Re\{\hat{P}_z\}$	$\Im\{\hat{P}_z\}$
S outer	-4.79E-05	2.67E-04	-1.08E-01	1.60E-01	-6.66E-07	-6.72E-07
S clearance	-1.13E-06	8.40E-06	-6.24E-03	2.61E-02	-7.62E-06	-2.30E-06
S inner	2.85E-04	-1.75E-03	-4.20E-02	**9.99E-01**	-8.51E-06	5.74E-06